I&EC research
Industrial & Engineering Chemistry Research
pubs.acs.org/IECR
Article

Al- and Nb-Comodified Ni-Rich NCM Cathode for High-Performance Lithium-Ion Batteries

Chengxin Zhu, Mengyao Xu, Kai Huang, Cheng Lian, Haiping Su,* and Honglai Liu

Cite This: *Ind. Eng. Chem. Res.* 2024, 63, 2740−2749
Read Online

ABSTRACT: Layered cathodes with a high nickel content (Ni ≥ 80%) are viewed as the ideal choice for the future of lithium-ion batteries (LIBs) because of their high specific capacity. However, the bad cyclic and thermal stability impedes its promotion because of the increase in the nickel content. Herein, it has been demonstrated that Al- and Nb-codoped $LiNi_{0.83}Co_{0.12}Mn_{0.05}O_2$ (NCM83-NA) can improve the structural stability and inhibit the release of lattice oxygen. It is found that the introduction of Al and Nb enlarges the interlayer spacing, and Nb ions induce the formation of radially oriented primary particles, which facilitate faster lithium-ion diffusion kinetics. XRD and XPS indicate that Al and Nb codoping reduces Li^+/Ni^{2+} cation mixing, Ni^{3+} with Jahn−Teller activity, and irreversible phase transition and increases the lattice oxygen content on surface. These endow materials with more stable structures and fewer surface side reactions. Consequently, NCM83-NA exhibits remarkable capacity retention (95.10% for 100 cycles at 1C), along with a notably enhanced rate capability, achieving 145.0 mA h g^{-1} at 5C. This work provides a hopeful approach for developing cathode materials with high performance.

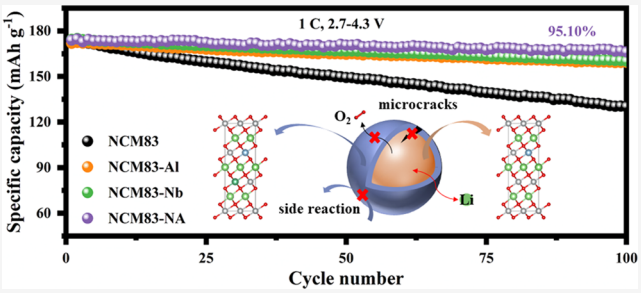

INTRODUCTION

Lithium-ion batteries (LIBs) are widely used because of their high energy density, low pollution, and other advantages.[1−3] However, in recent times, LIBs have struggled to fulfill the increasing energy density requirements.[4] The performance of LIBs, especially their energy density, is largely dependent on the cathode materials.[5] The Ni-rich layered oxide cathode is considered the preferred material of power batteries because of its high energy density.[6] However, the unsatisfied cyclic and thermal stability hinders its large-scale application.[7,8] The poor performance of the Ni-rich cathode comes from the lattice strain generated during cycling and the release of lattice oxygen.[9,10] When the voltage exceeds 4.1 V, the lattice of the material undergoes severe anisotropic volume contraction and local stress concentration due to the irreversible phase transition.[11,12] After long-term cycling, microcracks occur on the particle surface, ultimately leading to the rupture of particles.[13,14] These increase the cathode surface side reactions, accelerating the aging of the battery.[15,16] In addition, the release of lattice oxygen in the high lithium removal state not only affects the thermal safety of the battery but also increases the degree of lithium nickel mixing, hindering the transportation of lithium ions.[17,18]

To suppress the lattice strain and the lattice oxygen release, doping is the most used strategy. Various anions and cations doped at different sites, such as lithium sites (Na^+,[8] Mg^{2+},[19] Zn^{2+}[20]), transition metal (TM) sites (Zr^{4+},[21] Ta^{5+},[22] W^{6+}[23]), and oxygen sites (F^-,[24] Cl^-,[25] S^{2-}[26]), form stronger metal−oxygen bonds and ordering primary particles. The advantages of doping lie in three aspects: (1) replacing unstable Li/Ni/O elements with structurally stable elements; (2) restraining the undesirable phase transition to the rock-salt phase; and (3) forming more stable bonds between transition metals and oxygen (TM−O bonds) to decrease oxygen release. For example, elements with high solubility can improve the bulk phase structural stability of the cathode, but cannot suppress the surface side reactions effectively.[27] High valence ions can induce radially oriented primary particles, but it is difficult to diffuse into the bulk phase.[28] However, single-element doping cannot comprehensively solve various defects. Therefore, multielement doping is more promising in solving various problems of Ni-rich cathodes simultaneously.[29,30] Lu et al.[31] reported a Ni-rich cathode codoped with Al and Zr. The codoped materials exhibit faster lithium-ion migration and less internal strain and cation mixing. Sun et al.[32] synthesized bulk/surface-comodified $LiNi_{0.9}Co_{0.09}Mo_{0.01}O_2$ (NCMo90) through one-step calcination. This multifunctional structure maintains structural integrity during cycling effectively, exhibiting excellent capacity retention and rate performance.

Received: December 3, 2023
Revised: January 14, 2024
Accepted: January 18, 2024
Published: January 31, 2024

https://doi.org/10.1021/acs.iecr.3c04271
Ind. Eng. Chem. Res. 2024, 63, 2740−2749

Here, Al- and Nb-codoped $LiNi_{0.83}Co_{0.12}Mn_{0.05}O_2$ (NCM83) was synthesized by a solid-state method. Al is the most widely studied dopant, which can significantly improve the structural stability and conductivity. The Al−O bond has a formation energy higher than that of the Ni−O bond, which can inhibit the release of lattice oxygen. Nb^{5+} is beneficial for the formation of radially arranged primary particles.[33] In addition, Nb doping can reduce Ni^{3+} with Jahn−Teller activity and stabilize the lattice oxygen. Attributed to the bulk-to-surface modification of Al and Nb, modified NCM83 exhibited a better performance. First, the doping formation energy of Al and Nb ions was calculated, which demonstrated that the Al ion tends to enter the bulk, but the Nb ion is more likely to be doped on the subsurface. Subsequently, NCM83 with Al and Nb comodification was synthesized. The introduction of Al and Nb atoms from bulk to surface contributes to the enlarged interlayer space and stronger TM−O and suppresses internal intrinsic stress, thus increasing the lithium-ion diffusion kinetics, reducing the cation mixing and phase transition. Therefore, the NCM83-NA cathode exhibits a comprehensively improved cyclic stability (95.10% retention for 100 cycles at 1C) and rate capability (145.0 mA h g^{-1} at 5C).

■ METHODS

Material Preparation. The $Ni_{0.83}Co_{0.12}Mn_{0.05}(OH)_2$ precursor was purchased from Guangzhou Lige Technology Co., Ltd. All Ni-rich cathodes were prepared by a calcination method with $Ni_{0.83}Co_{0.12}Mn_{0.05}(OH)_2$, $LiOH{\cdot}H_2O$, $Al(OH)_3$, or/and Nb_2O_5 as raw materials. To obtain the Al- and Nb-codoped material, the precursor was mixed with $Al(OH)_3$, Nb_2O_5, and $LiOH{\cdot}H_2O$ (Li:TM:Al:Nb = 1.05:1:0.015:0.005). The mixture underwent a preheating process at 500 °C for 6 h, followed by calcination at 800 °C for 12 h under an O_2 atmosphere. For comparison, pristine NCM83 and Al-doping and Nb-doping NCM83 materials were synthesized by the same method. The products were defined as NCM83-Al, NCM83-Nb, and NCM83-NA, respectively.

Material Characterization. The element content of all cathodes was identified by inductively coupled plasma atomic emission spectrometry (ICP-OES, Agilent 5800). Microstructures of all cathodes were analyzed by field emission scanning electron microscopy (FESEM, Gemini SEM 500) and high-resolution transmission electron microscopy (HRTEM, FEI Talos F200X). The cross-sectional morphology was characterized by a focused ion beam etching technique (FIB, TESCAN GALA 3). Element distribution was analyzed by SEM equipped with energy-dispersive X-ray spectroscopy (EDS). The crystalline structure of all cathodes was characterized by X-ray diffraction (XRD, Bruker D8 Advance), and the results were analyzed with the GSAS Rietveld refinement software. The element oxidation state was characterized by X-ray photoelectron spectrometery (XPS, Thermo Scientific K-α).

Electrochemical Test. The electrochemical performance of all materials was assessed in half-cells (CR2016 coin-type). The materials were combined with Super-P and poly(vinylidene fluoride) (PVDF) in 8:1:1 wt %, using *N*-methyl-2-pyrrolidone (NMP) as the solvent. Then, the slurry was applied to aluminum foil and vacuum-dried, achieving a mass loading of 2.0 mg cm^{-2}. The electrolyte was 1.0 M $LiPF_6$ in EC:DMC:EMC = 1:1:1 vol %, the counter electrode was lithium plates, and the separator was Celgard 2400 polypropylene. For the full-cells, the counter electrode was replaced by commercial graphite and the N/P areal capacity ratio was controlled to be 1.15−1.20. The LANDCT2001A test system was used to conduct galvanostatic charge−discharge tests of half- and full-cells. The galvanostatic intermittent titration technique (GITT) test was carried out with a 2 h relaxation time after charging/discharging for 20 min at 0.1C (1C = 200 mA g^{-1}). Cyclic voltammetry (CV) with different scan rates was conducted on the CHI604E electrochemical workstations. Electrochemical impedance spectroscopy (EIS) was conducted over a frequency spectrum ranging from 100−0.01 kHz. To evaluate the cathodes after cycling, the electrode plates were removed and dried after being washed with dimethyl carbonate.

Theoretical Calculations. Density functional theory (DFT) was performed using the Vienna ab initio simulation package (VASP).[34] Generalized gradient approximation (GGA) within the Perdew−Burke−Ernzerhof (PBE)[35] function was employed. The projector augmented wave (PAW)[36] method and plane wave basis sets were employed. The GGA + D3[37] approach was used to incorporate dispersion corrections. The plane wave cutoff energy was 500 eV. The structures were optimized by minimizing the forces on all of the atoms to <0.03 eV $Å^{-1}$ and the energy to $<10^{-5}$ eV. The K point adopted the density of 4*4*2. To assess the doping energies of pristine and doped $LiNiO_2$, the 3 × 3 × 1 supercell with appropriate lattice parameters was utilized, and Al and Nb were substituted with nickel sites in the transition layers. The doping formation energy (ΔE) of Al or Nb was defined as

$$\Delta E = E_{\text{doped}} + \mu_{\text{Ni}} - E_{\text{pristine}} - \mu_{\text{A}} \tag{1}$$

where element A could be Al or Nb. E_{doped} and E_{pristine} were the energies of doped and pristine $LiNiO_2$, respectively. μ_{Ni} and μ_{A} were the chemical potentials of substituted and replaced elements calculated in its most stable bulk form, respectively. The oxygen vacancy formation energy (ΔE) was defined as

$$\Delta E = E_{V_{\text{O}}} - E_{\text{pristine}} + \frac{1}{2}\mu_{\text{O}_2} \tag{2}$$

where $E_{V_{\text{O}}}$ and E_{pristine} were the total energies of the oxygen vacancy and pristine structure, respectively. μ_{O_2} was the chemical potential of O_2. Furthermore, the climbing image-nudged elastic band (CI-NEB) method[38] was performed to obtain the Li-ion diffusion energy barrier.

■ RESULTS AND DISCUSSION

Density functional theory (DFT) was used to evaluate the structural stability of $LiNiO_2$ doped with different atoms.[39,40] As indicated in Figure S1, the first layer of the structure is defined as the surface, while the other layers away from the vacuum layer are defined as the bulk phase. The third layer is fixed with the bulk lattice. It clearly shows that Al was doped in the bulk and Nb was doped on the surface. As shown in Figure S2, the Al ions are apt to enter the bulk phase due to the high solubility in $LiNiO_2$, which exhibits a much lower formation energy of −6.10 eV. In contrast, the Nb ions in the surface layer of $LiNiO_2$ are structurally stable.[41]

As the structure and electrochemical performance are related to surface lattice oxygen, the oxygen vacancy formation energies (ΔEs) have been analyzed (Figure S3a,b). Here, oxygen vacancies are located at the junction vertex of three adjacent MO_6 octahedra. The calculated ΔE values are 1.29, 1.92, and 2.56 eV for $LiNiO_2$, Al-$LiNiO_2$, and Nb-$LiNiO_2$,

https://doi.org/10.1021/acs.iecr.3c04271
Ind. Eng. Chem. Res. 2024, 63, 2740−2749

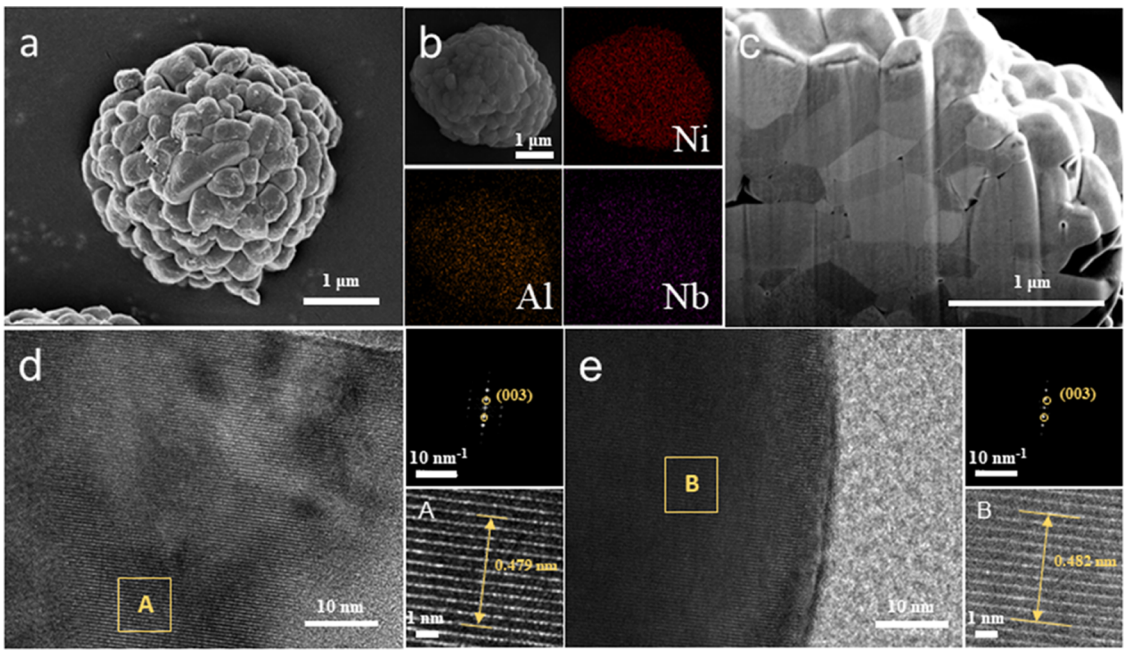

Figure 1. (a) SEM image of NCM83-NA. (b) The corresponding EDS mapping images of NCM83-NA. (c) Cross-sectional SEM image of NCM83-NA. High-resolution TEM images of (d) NCM83 and (e) NCM83-NA.

respectively. The interaction between Al/Nb and O is stronger than Ni and O, which can effectively suppress the irreversible structural transition.[32] Furthermore, the Li-ion diffusion energy barrier during the charging process was calculated (Figure S3c,d). Compared to NCM83, the Li^+ migration energy barrier is reduced by 0.08 and 0.09 eV for Al-$LiNiO_2$ and Nb-$LiNiO_2$, respectively. A lower migration energy barrier improves the migration rate of Li^+ and is propitious to the rate capabilities of the lithium-ion battery.[42] Therefore, materials codoped with Al and Nb are expected to exhibit an excellent cycling stability and rate performance.

The Al/Nb-doped cathodes were synthesized by a calcination method. Al and Nb in the cathode materials were measured by ICP-OES (Table S1), which is in accord with the target proportion. Figure S4 shows the SEM images of NCM83 and doped materials. It shows that there are no substantial morphology differences before and after doping, both of which are spherical particles of about 5 μm. As shown in Figure 1a, NCM83-NA maintains the sphere structure with nanoscale primary particles. The corresponding EDS mapping (Figure 1b) indicates that Al and Nb are uniformly doped in NCM83-NA, where Al was supposed to distribute in the bulk, while Nb was on the surface. The cross-sectional SEM image shown in Figure 1c suggests NCM83-NA with radially oriented primary particles, which provides a fast transport channel for lithium ions.[43,44] In addition, the HRTEM images of NCM83 (Figure 1d) and NCM83-NA (Figure 1e) clearly show that the interplanar interval of the (003) plane increased from 0.479 to 0.482 nm, directly proving the successful introduction of heteroatoms into NCM83. The increased lattice spacing will promote the migration of Li ions.[45]

Figure 2a is the structural diagram of NCM83-NA with Al and Nb doped on the surface and bulk. The stable configuration of Al and Nb doped at the Ni position did not alter the layered structure of $LiNiO_2$. Figure 2b−e are the XRD results of the materials. Obviously, both NCM83 and codoped NCM83-NA exhibit a α-$NaFeO_2$ structure. The intensity of (003) and (104) peaks is high, and (006)/(102) and (018)/(110) peaks clearly split, demonstrating that the doped material maintains a high degree of crystallinity.[46] Specifically, the (003) peak of NCM83-NA shifts to a smaller angle, indicating the enlargement of the interlayer spacing. As depicted in Figure 2e, the intensity ratio of the (003)/(104) peak increases as Al and Nb are introduced, indicating the reduction of cation mixing.[47] The corresponding XRD Rietveld refinement data given in Figures 2f and S6 and Table S2 show that the c lattice parameters are conspicuously enlarged and the Li/Ni disorder reduces significantly. In addition, due to the embedding of Al and Nb, the TM layer shrinks and the Li layer expands. After doping, the interlayer spacing of the TM layer decreased from 2.12A to 2.11A, while the interlayer spacing of Li layer increased from 2.58A to 2.68A.[48]

The oxidation state of elemental materials was characterized by XPS (Figures 2g−j and S7 and S8). The peaks at 855.28 and 872.88 eV correspond to Ni $2p_{3/2}$ and Ni $2p_{1/2}$, respectively (Figure 2g). The Ni $2p_{3/2}$ peak can split to Ni^{3+} at 856.28 eV and Ni^{2+} at 854.98 eV. Compared to that of NCM83, the proportion of Ni^{2+} for NCM83-NA increases because of charge compensation. It is worth noting that Ni^{3+} is an ion with Jahn−Teller activity, and the increase in Ni^{3+} will lead to irreversible structural transformations in the material. Among all of the samples, the NCM83-NA material has the least Ni^{3+} content, indicating the best structural stability.[49] For Nb 3d (Figure 2h) and Al 2p (Figure 2i) XPS spectra, the main peaks at 208.98, 206.18, and 72.18 eV are identified as Nb $3d_{5/2}$, Nb $3d_{3/2}$, and Al 2p, revealing that Al and Nb exist as Al^{3+} and Nb^{5+} in the material, respectively. Figure 2j exhibits the spectra of O 1s of NCM83 and NCM83-NA. The peaks at 531.58 and 528.98 eV correspond to the reactive oxygen and lattice oxygen bonds on the surface, respectively.[50] The peak intensity of TM−O in NCM83-NA is significantly stronger than that in NCM83, indicating that Al/Nb can suppress the formation of oxygen vacancies.[51−53] In addition, the doping of Al and Nb ions decreases the amount of surface residual

https://doi.org/10.1021/acs.iecr.3c04271
Ind. Eng. Chem. Res. 2024, 63, 2740−2749

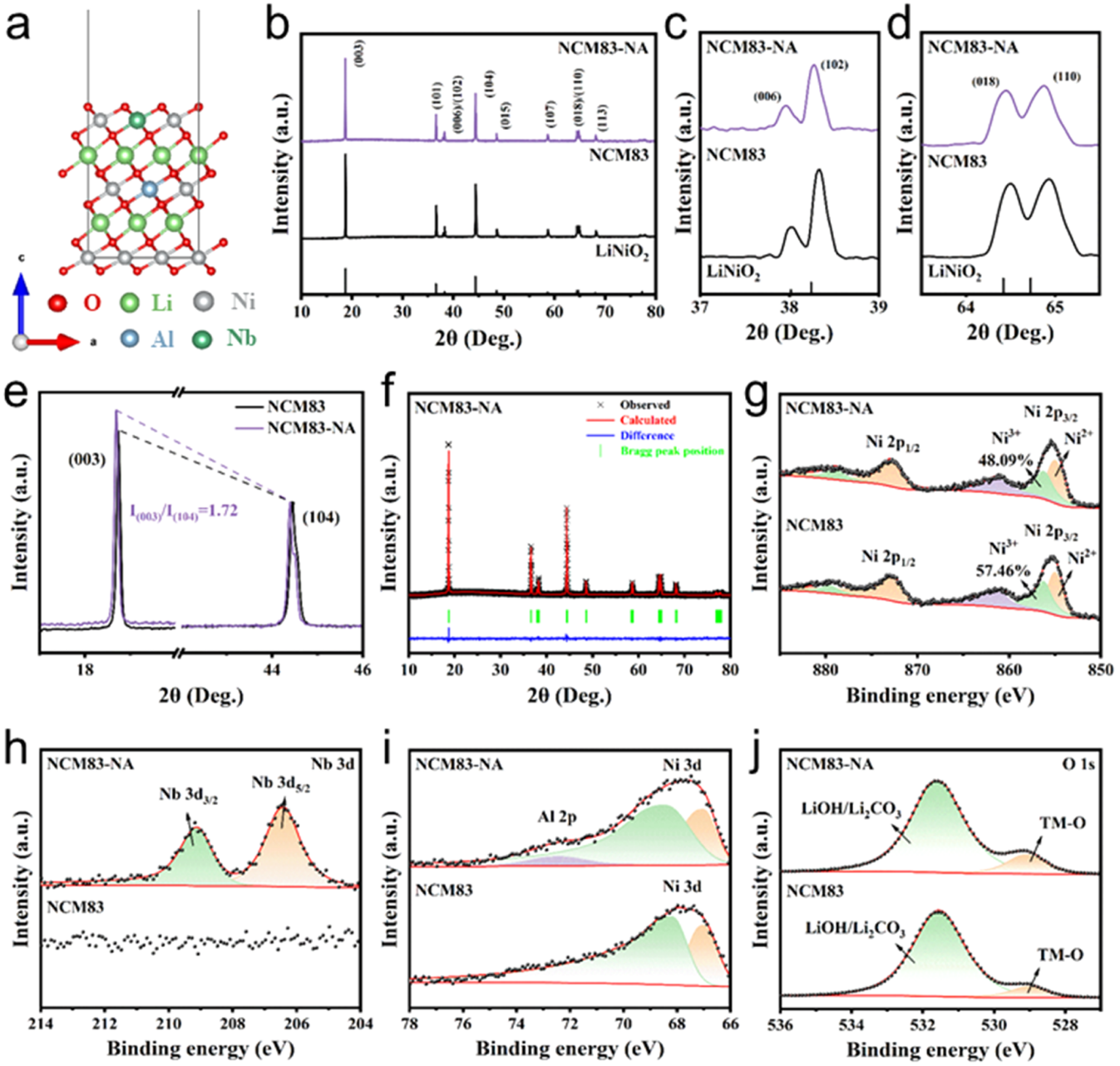

Figure 2. (a) Structure diagram of NCM83-NA. (b) XRD patterns of NCM83 and NCM83-NA with the magnification region of (c) (006)/(102) and (d) (018)/(110) peaks. (e) (003) and (104) XRD peaks of NCM83 and NCM83-NA after normalizing the (104) peak. (f) Rietveld refinement results for NCM83-NA. XPS results of (g) Ni 2p, (h) Nb 3d, (i) Al 2p, and (j) O 1s for NCM83 and NCM83-NA.

lithium compounds. The peaks at 780.28 and 795.18 eV are associated with Co $2p_{3/2}$ and Co $2p_{1/2}$, respectively.[51] The peaks at 642.18 and 654.68 eV are associated with Mn $2p_{3/2}$ and Mn $2p_{1/2}$, respectively.[49] There are no obvious changes in the Co 2p and Mn 2p spectra, indicating that Al and Nb doping has no effect on Co and Mn ions.

The electrochemical performance of all materials is evaluated by coin-type half- and full-cells. The initial charge−discharge curves at 0.1C within 2.7−4.3 V for all samples are shown in Figure 3a. NCM83-NA displays a discharge capacity of 195.1 mA h g^{-1} and a higher initial Coulombic efficiency (ICE) of 96.21%. The ICEs are 91.87, 95.92, and 96.02% for NCM83, NCM83-Al, and NCM83-Nb, respectively. The increased ICE indicates that NCM83-NA has a more stable structure and a suppressed side reaction on the surface. As shown in Figure 3b, after 100 cycles at 1C, the capacity retention ratio of Al- or/and Nb-doped NCM83 has significantly improved. Specially, NCM83-NA exhibits the highest capacity retention rate of 95.10%. The Nyquist plots of electrochemical impedances at the fully charged state (4.3 V) are provided in Figure 3c. The solution resistance (R_u) for all samples was approximately 5 Ω. NCM83-NA shows the smallest surface-film impedance (R_{sf}) of 9.83 Ω and charge-transfer impedance (R_{ct}) of 19.52 Ω, illustrating that Al and Nb doping is beneficial to forming more stable cathode−electrolyte interface (CEI) films because of reduced parasitic reactions. The rate performance of all materials at 0.1−5C is shown in Figure 3d. The discharge capacities of doped materials have a slight decrease at 0.1C. However, NCM83-NA shows a higher specific capacity than that of NCM83 with the

https://doi.org/10.1021/acs.iecr.3c04271
Ind. Eng. Chem. Res. 2024, 63, 2740−2749

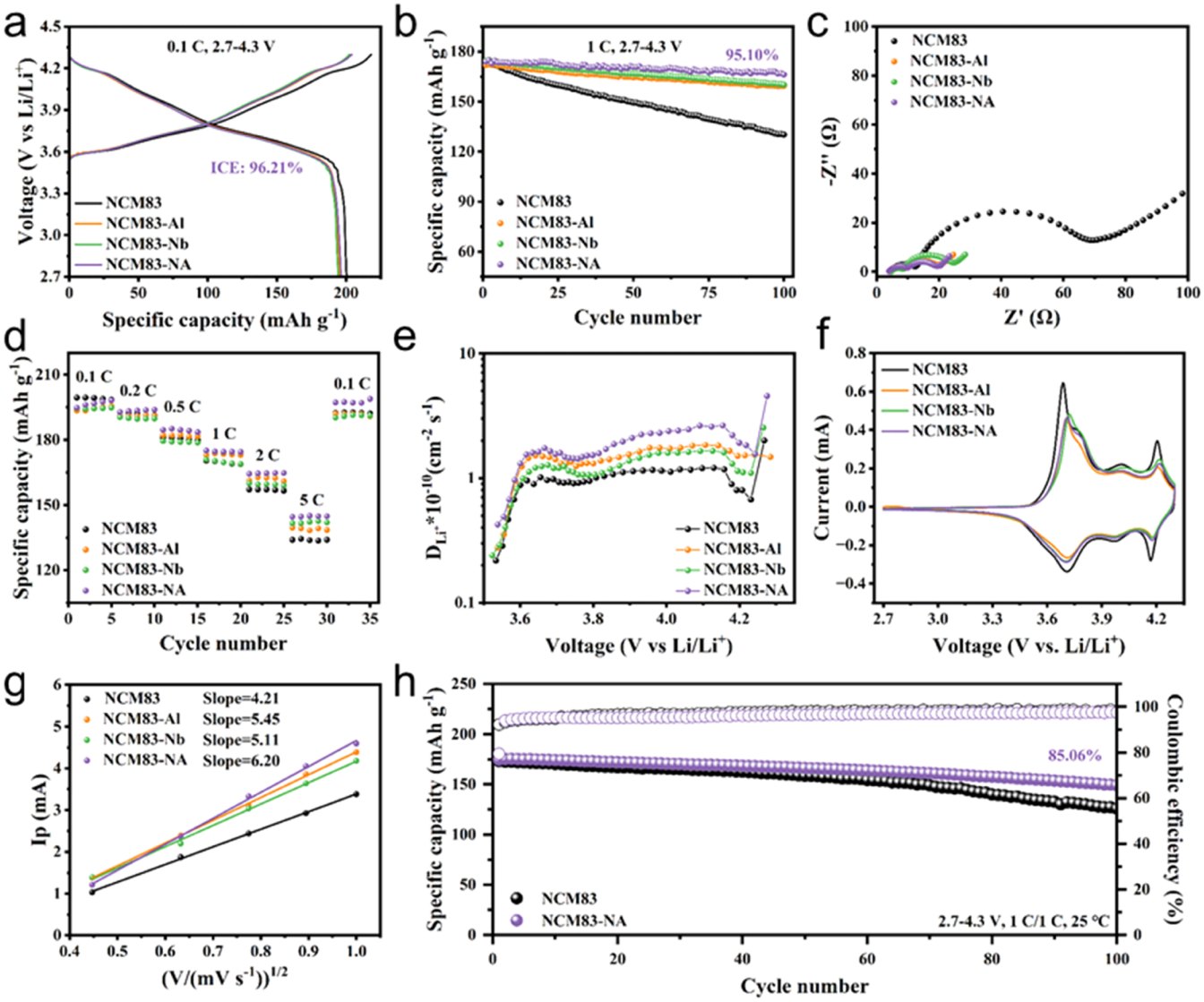

Figure 3. (a) Initial charge−discharge curves. (b) Cycling stability. (c) Nyquist plots of electrochemical impedances at 4.3 V. (d) Rate performance at 0.1−5C. (e) Lithium-ion diffusion coefficient of charging curves according to GITT data. (f) CV curves at 0.1 mV s^{-1}. (g) Relationship between the peak current and the scanning rate. (h) Cycling stability of full-cells.

increase of current densities. Peculiarly, NCM83-NA displays a superior capacity of 145.0 mA h g^{-1} at 5C, while NCM83 delivers a lower capacity of 133.5 mA h g^{-1}. The specific capacity of Al- or Nb-doped NCM83 at 5C is around 140 mA h g^{-1}. Besides, the discharge capacity of NCM83-NA can instantly recover to 197.2 mA h g^{-1} once the current density reduces back to 0.1C. To further understand the better rate performance of NCM83-NA, GITT tests are conducted to measure the diffusion coefficient of lithium ions (Figures 3e and S10). NCM83-NA possesses the fastest Li^+ diffusion kinetics, thereby leading to a superior rate capability. Meanwhile, the CV curves at 0.1−1.0 mV s^{-1} and the linear relationship between the peak current (i_p) and the square root of the scan rate ($v^{1/2}$) for all materials are given (Figures 3f,g and S10). As shown in Figure 3f, all materials have good symmetry in their CV curves. NCM83-NA shows the largest slope of 6.20, indicating the significantly enhanced Li^+ diffusion rate and reaction kinetics, which is consistent with the GITT results.[62,63] It is because Al and Nb introduction enlarged the lattice parameters, which can facilitate the Li^+ diffusion.[64,65] To better assay the electrochemical performance of NCM83-NA, full-cells were tested. As shown in Figure 3h, the capacity retention ratio of NCM83-NA remains at 85.0% after 100 cycles at 1C, which is much higher than that of NCM83 (72.7%). Compared with the research published in recent years, NCM83-NA exhibits an excellent capacity retention after 100 cycles (Table 1).

Figures 4a and S11 compare the charge−discharge curves of all materials from first to 100th cycles. Obviously, NCM83-NA shows an excellent capacity retention ratio and voltage profile stability. The CV curves at 0.1 mV s^{-1} of the second and 100th cycles are shown in Figure S12, which show that the curve evolution of NCM83-NA is nearly negligible, indicating a significantly enhanced structural stability.[66,67] The Nyquist plots of electrochemical impedances after first and 100th cycles are provided in Figure 4b, and the corresponding R_u, R_{sf}, and R_{ct} values are displayed in Table S3. After 100 cycles, the changes in R_u were negligible. The R_{ct} for NCM83, NCM83-Al, NCM83-Nb, and NCM83-NA are 314.7, 103.1, 101.6, and 60.7 Ω, respectively, illustrating that NCM83-NA inhibits

https://doi.org/10.1021/acs.iecr.3c04271
Ind. Eng. Chem. Res. 2024, 63, 2740−2749

Table 1. Half-Cell Performance of Ni-Rich Cathodes

reference	rate	cutoff voltage	number of cycles	capacity retention
ref 1[1]54	0.5C	3.0−4.3 V	100	90.4%
ref 2[2]41	1C	2.75−4.3 V	100	91.10%
ref 3[3]55	0.5C	2.7−4.3 V	100	91.9%
ref 4[4]56	1C	2.7−4.3 V	100	88.5%
ref 5[5]57	0.5C	3.0−4.3 V	100	86.3%
ref 6[6]58	0.5C	2.7−4.3 V	100	95.44%
ref 7[7]59	0.5C	3.0−4.3 V	100	91.40%
ref 8 60	0.33C	3.0−4.3 V	100	91.00%
ref 9[9]61	0.5C	2.8−4.3 V	100	89.77%
this work	1C	2.7−4.3 V	100	95.10%

interface side reactions during continuous cycling effectively. In addition, dQ/dV is conducted to clarify the structure evolution after cycling (Figures 4c and S13). During the charge process, both NCM83 and NCM83-NA take a series of phase transitions: from the hexagonal phase (H1) to the monoclinic phase (M) and two other hexagonal phases (H2 and H3). The phase between H2 and H3 is closely related to the contraction or expansion of the Li−O layer, which may lead to intergranular cracking of cathode particles.[68] NCM83-NA shows a much better reversibility of the phase between H2 and H3, explaining its obviously improved cycling stability.

To investigate the dynamic crystal structure evolution during the delithiation/lithiation process, ex situ XRD for NCM83 and NCM83-NA is conducted. The variation of the (003), (101), (102), (104), and (110) peaks in both materials is shown in Figure 4d,e. When the voltage increased to 4.1 V, the (003) peak shifted to a lower 2θ accompanied by the delithiation process and phase transition from H1 to M and H2, illustrating the lattice expansion along with the c-axis. As the voltage increased to 4.3 V, the (003) peak quickly shifted to a higher 2θ because of the phase transition from H2 to H3, indicating the lattice contraction in the c-axis direction.[31,50] During the lithiation process, the phase underwent a reverse transition. The shift angles of the H2−H3 phase transition are 0.32 and 0.2° for NCM83 and NCM83-NA, respectively, which means the doped Ni-rich cathode has a smaller volume

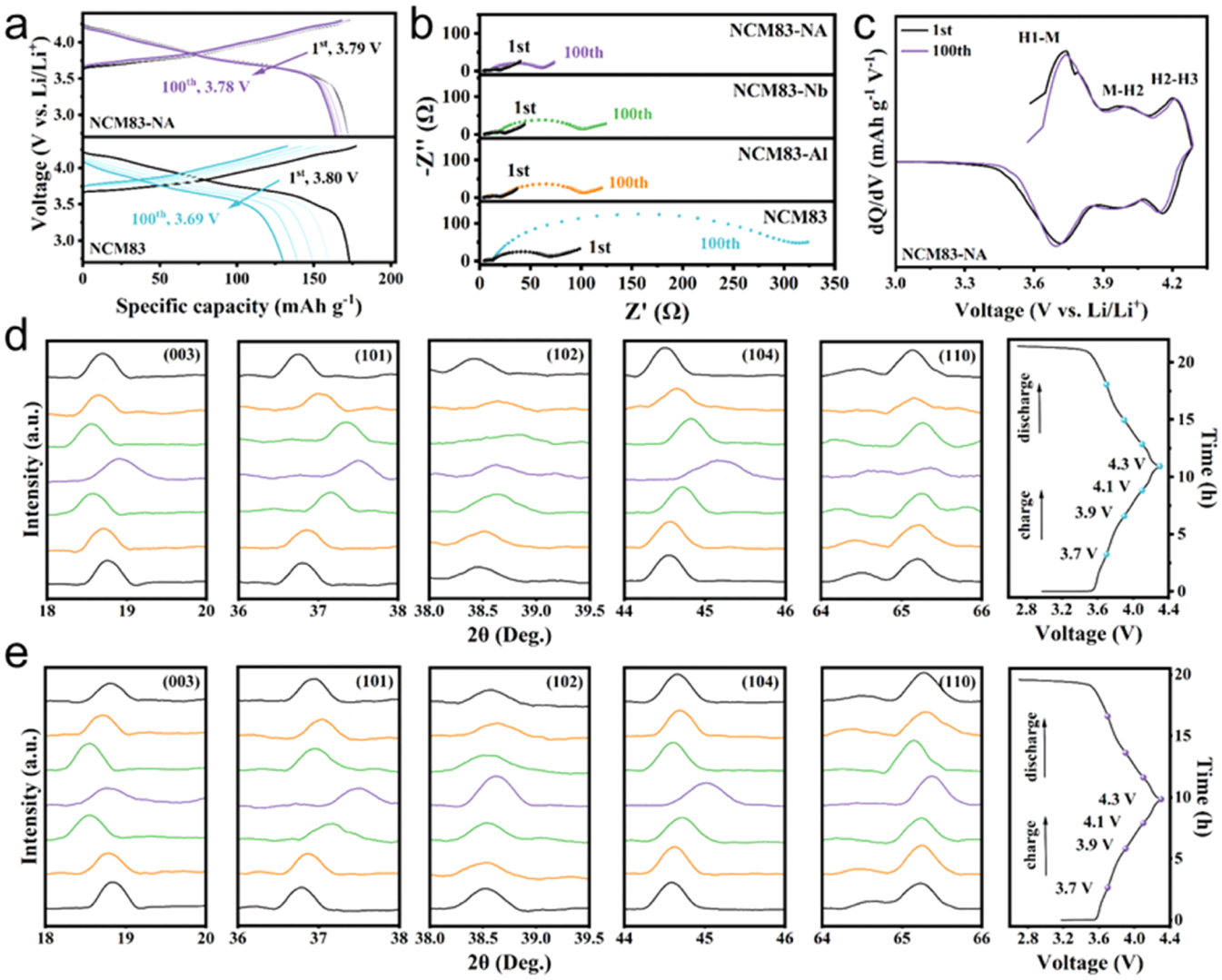

Figure 4. (a) Charge−discharge profiles of NCM83 and NCM83-NA with different cycles at 1C. (b) Nyquist plots of electrochemical impedances at the fully charged state (4.3 V) after different cycles. (c) Calculated dQ/dV curves of NCM83-NA by differentiating charge−discharge curves. Ex situ XRD contour plots of (003), (101), (102), (104), and (110) peaks with the corresponding charge−discharge curves for (d) NCM83 and (e) NCM83-NA.

https://doi.org/10.1021/acs.iecr.3c04271
Ind. Eng. Chem. Res. 2024, 63, 2740−2749

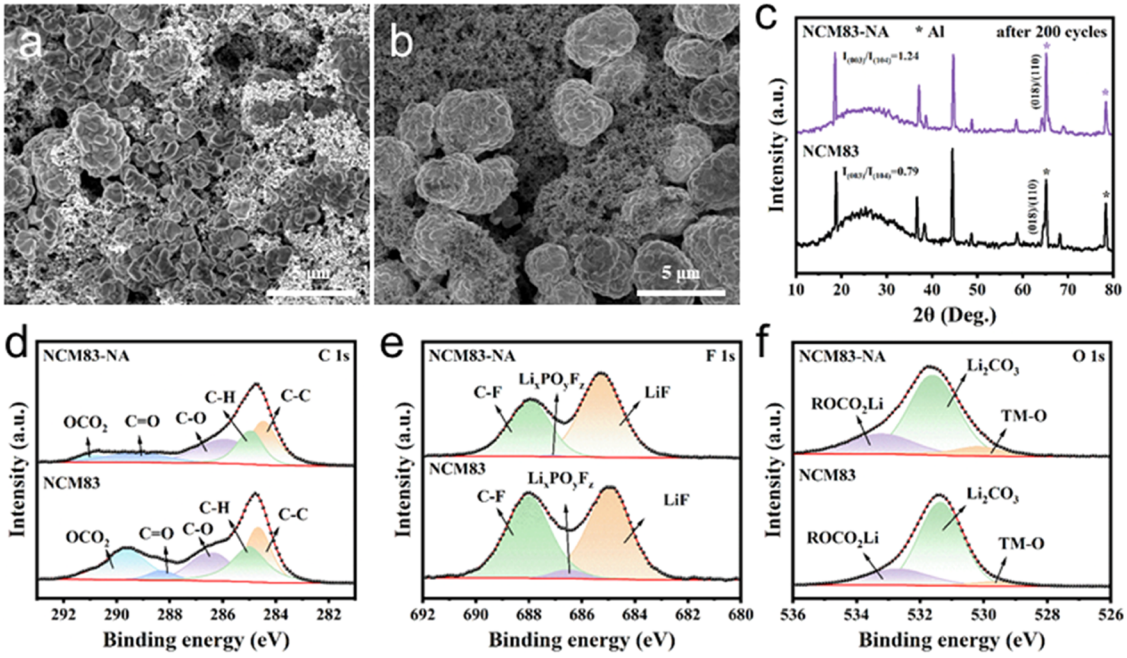

Figure 5. SEM images of (a) NCM83 and (b) NCM83-NA after 100 cycles. (c) XRD patterns of NCM83 and NCM83-NA after 100 cycles. XPS spectra of (d) C 1s, (e) F 1s, and (f) O 1s for NCM83 and NCM83-NA after 100 cycles.

change and a better structural stability. In addition, the (101), (102), (104), and (110) peaks gradually shift to a higher 2θ with increasing voltage. The angles of transformation also decrease, illustrating the improvement of the structural stability during cycling after Al and Nb ions are introduced.

To explore the deterioration mechanism of the cathodes, the postmortem analyses including SEM, XRD, and XPS were conducted. The SEM images of NCM83 and NCM83-NA after 100 cycles are shown in Figures 5a,b and S14 to visually detect the particle integrity. For NCM83, a large number of particle fractures are observed. In contrast, particles of NCM83-NA maintain well, indicating Al and Nb ion doping enhances the connection between primary particles and the cycling stability. It is noted that particle fracture increases the contact area between the active material and the electrolyte, thus increasing side reactions on the surface. In the XRD spectra (Figure 5c), the $I_{(003)}/I_{(104)}$ ratios are 0.79 and 1.24 for NCM83 and NCM83-NA, respectively, suggesting the more severe irreversible phase transitions and the structure destruction for NCM83. In addition, the (018) and (110) peaks of NCM83 almost blend together, indicating the collapse of its layered structures. The obvious splitting of (018)/(110) peaks of NCM83-NA was still observed after 100 cycles, implying that the pinning effect of Al and Nb ions reduces the mechanical strain. The electrolyte decomposition production of cycled NCM83 and NCM83-NA is examined by XPS (Figure 5d−f). The C 1s spectrum can be divided into five peaks: C−C at 284.46 eV, C−H at 284.80 eV, C−O at 286.17 eV, C═O at 288.10 eV, and OCO_2 at 289.39 eV. Among them, C−C and C−H peaks are related to the binder and Super-P, while C−O, C═O, and OCO_2 peaks are associated with the lithium alkyl carbonates ($ROCO_2Li$, ROLi, and Li_2CO_3) that are attributed to the dissolution of carbonate electrolyte solvents. Compared to NCM83, the area proportion of C−O, C═O, and OCO_2 peaks for NCM83-NA reduces from 43.37 to 34.59%, which indicates the presence of more organic components from the electrolyte decomposition on the surface of NCM83. In the F 1s spectra, the peaks located at 684.85, 686.49, and 687.08 eV correspond to LiF, $Li_xPO_yF_z$, and C−F. The $Li_xPO_yF_z$ content reduced from 3.55 to 0.59%, implying that the side reactions of the electrolyte are greatly reduced. Moreover, the increase of inorganic component LiF from 50.76 to 59.17% endows the cathode particle surface with a more robust CEI.[69] In addition, the increased proportion of the M−O peak at 529.58 eV in the O 1s spectra from 4.41 to 9.46% illustrates a suppressed release of lattice oxygen on the surface (Figure 5f). Thus, these data verify that Al and Nb codoping can improve the structural stability by reducing the electrolyte decomposition and lattice oxygen release during cycling.

■ CONCLUSIONS

In this work, Al- and Nb-doped $LiNi_{0.83}Co_{0.12}Mn_{0.05}O_2$ has been successfully synthesized by a solid-state reaction method. Both experimental and theoretical data demonstrate improved structural stability and lithium-ion diffusion kinetics. Specifically, NCM83-NA exhibits a better cyclic stability and rate performance than single Al- or Nb-doped materials. It shows a discharge capacity of 196.6 mA h g^{-1} and maintains a capacity retention rate of 95.10% at 1C after 100 cycles in the voltage range of 2.7−4.3 V. At a higher current density of 5C, it delivers a discharge capacity of 145.0 mA h g^{-1}. The excellent performance can be attributed to the following factors: (1) the introduction of Nb ions induces the formation of radially oriented primary particles; (2) Al and Nb doping enlarges the interlayer spacing; (3) Al and Nb ions reduce Li^+/Ni^{2+} cation mixing and Ni^{3+} with Jahn−Teller activity; (4) the stronger Al−O and Nb−O bonds lower oxygen vacancies; and (5) the irreversible H2−H3 phase transition is suppressed. These factors lead to a more stable structure and faster Li^+ diffusion of NCM83-NA. Overall, this work provides a promising solution to developing Ni-rich cathode materials with high cycling stability and rate capability.

https://doi.org/10.1021/acs.iecr.3c04271
Ind. Eng. Chem. Res. 2024, 63, 2740−2749

■ ASSOCIATED CONTENT

Supporting Information

The Supporting Information is available free of charge at https://pubs.acs.org/doi/10.1021/acs.iecr.3c04271.

Model and results of DFT calculations, additional results of ICP-OES, SEM image, XRD and the corresponding Rietveld refinement, and XPS and electrochemical testing (PDF)

■ AUTHOR INFORMATION

Corresponding Author

Haiping Su − *School of Chemistry and Molecular Engineering, East China University of Science and Technology, Shanghai 200237, China;* orcid.org/0000-0003-4744-9692; Email: hpsu@ecust.edu.cn

Authors

Chengxin Zhu − *State Key Laboratory of Chemical Engineering, School of Chemical Engineering, East China University of Science and Technology, Shanghai 200237, China*

Mengyao Xu − *School of Chemistry and Molecular Engineering, East China University of Science and Technology, Shanghai 200237, China*

Kai Huang − *School of Chemistry and Molecular Engineering, East China University of Science and Technology, Shanghai 200237, China*

Cheng Lian − *State Key Laboratory of Chemical Engineering, School of Chemical Engineering, East China University of Science and Technology, Shanghai 200237, China; School of Chemistry and Molecular Engineering, East China University of Science and Technology, Shanghai 200237, China;* orcid.org/0000-0002-9016-832X

Honglai Liu − *State Key Laboratory of Chemical Engineering, School of Chemical Engineering, East China University of Science and Technology, Shanghai 200237, China; School of Chemistry and Molecular Engineering, East China University of Science and Technology, Shanghai 200237, China;* orcid.org/0000-0002-5682-2295

Complete contact information is available at: https://pubs.acs.org/10.1021/acs.iecr.3c04271

Notes

The authors declare no competing financial interest.

The authors declare that theys have no known competing financial interests or personal relationships that could have appeared to influence the work reported in this paper.

■ ACKNOWLEDGMENTS

This work was sponsored by the National Key Research and Development Program of China (No. 2022YFA1503501), the State Key Laboratory of Clean Energy Utilization (Open Fund Project No. ZJUCEU2021005), and the Fundamental Research Funds for the Central Universities (2022ZFJH004). This work was supported by the 21C Innovation Laboratory, Contemporary Amperex Technology Ltd. (Project No. 21C-OP-202312).

■ REFERENCES

(1) Cheng, H.; Sun, Q.; Li, L.; Zou, Y.; Wang, Y.; Cai, T.; Zhao, F.; Liu, G.; Ma, Z.; Wahyudi, W.; Li, Q.; Ming, J. Emerging Era of Electrolyte Solvation Structure and Interfacial Model in Batteries. *ACS Energy Lett.* **2022**, *7* (1), 490−513.

(2) Chang, F.; Xiao, M.; Miao, R.; Liu, Y.; Ren, M.; Jia, Z.; Han, D.; Yuan, Y.; Bai, Z.; Yang, L. Copper-Based Catalysts for Electrochemical Carbon Dioxide Reduction to Multicarbon Products. *Electrochem. Energy Rev.* **2022**, *5* (3), No. 4, DOI: 10.1007/s41918-022-00139-5.

(3) Guo, J.-Z.; Gu, Z.-Y.; Du, M.; Zhao, X.-X.; Wang, X.-T.; Wu, X.-L. Emerging Characterization Techniques for Delving Polyanion-type Cathode Materials of Sodium-ion Batteries. *Mater. Today* **2023**, *66*, 221−244.

(4) Li, W.; Erickson, E. M.; Manthiram, A. High-nickel Layered Oxide Cathodes for Lithium-based Automotive Batteries. *Nat. Energy* **2020**, *5* (1), 26−34.

(5) Lee, S.; Hwang, J.; Park, C.; Ahn, S.; Do, K.; Kim, S.; Ahn, H. Efficient and Scalable Encapsulation Process of Highly Conductive 1T-MoS2 Nanosheets on Ni-rich $LiNi_{0.83}Co_{0.11}Mn_{0.06}O_2$ Cathode Materials for High-performance Lithium-ion Batteries. *Chem. Eng. J.* **2023**, *470*, No. 144209.

(6) Ni, L.; Chen, H.; Guo, S.; Dai, A.; Gao, J.; Yu, L.; Mei, Y.; Wang, H.; Long, Z.; Wen, J.; Deng, W.; Zou, G.; Hou, H.; Liu, T.; Amine, K.; Ji, X. Enabling Structure/Interface Regulation for High-Performance Ni-Rich Cathodes. *Adv. Funct. Mater.* **2023**, *33* (51), No. 2307126, DOI: 10.1002/adfm.202307126.

(7) Nam, G. W.; Park, N.-Y.; Park, K.-J.; Yang, J.; Liu, J.; Yoon, C. S.; Sun, Y.-K. Capacity Fading of Ni-Rich NCA Cathodes: Effect of Microcracking Extent. *ACS Energy Lett.* **2019**, *4* (12), 2995−3001.

(8) Shen, Y.; Yao, X.; Zhang, J.; Wang, S.; Zhang, D.; Yin, D.; Wang, L.; Zhang, Y.; Hu, J.; Cheng, Y.; Li, X. Sodium Doping Derived Electromagnetic Center of Lithium Layered Oxide Cathode Materials with Enhanced Lithium Storage. *Nano Energy* **2022**, *94*, No. 106900.

(9) Hou, D.; Xu, Z.; Yang, Z.; Kuai, C.; Du, Z.; Sun, C.-J.; Ren, Y.; Liu, J.; Xiao, X.; Lin, F. Effect of the Grain Arrangements on the Thermal Stability of Polycrystalline Nickel-rich Lithium-based Battery Cathodes. *Nat. Commun.* **2022**, *13* (1), No. 3437, DOI: 10.1038/s41467-022-30935-y.

(10) Kim, J.-H.; Ryu, H.-H.; Kim, S. J.; Yoon, C. S.; Sun, Y.-K. Degradation Mechanism of Highly Ni-Rich $Li[Ni_xCo_yMn_{1-x-y}]O_2$ Cathodes with $x > 0.9$. *ACS Appl. Mater. Interfaces* **2019**, *11* (34), 30936−30942.

(11) Fan, X.; Ou, X.; Zhao, W.; Liu, Y.; Zhang, B.; Zhang, J.; Zou, L.; Seidl, L.; Li, Y.; Hu, G.; Battaglia, C.; Yang, Y. In Situ Inorganic Conductive Network Formation in High-voltage Single-Crystal Ni-rich Cathodes. *Nat. Commun.* **2021**, *12* (1), No. 5320, DOI: 10.1038/s41467-021-25611-6.

(12) Xu, J.; Hu, E.; Nordlund, D.; Mehta, A.; Ehrlich, S. N.; Yang, X.-Q.; Tong, W. Understanding the Degradation Mechanism of Lithium Nickel Oxide Cathodes for Li-Ion Batteries. *ACS Appl. Mater. Interfaces* **2016**, *8* (46), 31677−31683.

(13) Zhang, S. S. Problems and Their Origins of Ni-rich Layered Oxide Cathode Materials. *Energy Storage Mater.* **2020**, *24*, 247−254.

(14) Su, Y.; Zhang, Q.; Chen, L.; Bao, L.; Lu, Y.; Chen, S.; Wu, F. Stress Accumulation in Ni-rich Layered Oxide Cathodes: Origin, Impact, and Resolution. *J. Energy Chem.* **2022**, *65*, 236−253.

(15) Zhao, W.; Zou, L.; Zhang, L.; Fan, X.; Zhang, H.; Pagani, F.; Brack, E.; Seidl, L.; Ou, X.; Egorov, K.; Guo, X.; Hu, G.; Trabesinger, S.; Wang, C.; Battaglia, C. Assessing Long-Term Cycling Stability of Single-Crystal Versus Polycrystalline Nickel-Rich NCM in Pouch Cells with 6 mAh cm^{-2} Electrodes. *Small* **2022**, *18* (14), No. 2107357, DOI: 10.1002/smll.202107357.

(16) Xu, C.; Märker, K.; Lee, J.; Mahadevegowda, A.; Reeves, P. J.; Day, S. J.; Groh, M. F.; Emge, S. P.; Ducati, C.; Layla Mehdi, B.; Tang, C. C.; Grey, C. P. Bulk Fatigue Induced by Surface Reconstruction in Layered Ni-rich Cathodes for Li-ion Batteries. *Nat. Mater.* **2021**, *20* (1), 84−92.

(17) Sun, C.; Liao, X.; Xia, F.; Zhao, Y.; Zhang, L.; Mu, S.; Shi, S.; Li, Y.; Peng, H.; Van Tendeloo, G.; Zhao, K.; Wu, J. High-Voltage Cycling Induced Thermal Vulnerability in $LiCoO_2$ Cathode: Cation Loss and Oxygen Release Driven by Oxygen Vacancy Migration. *ACS Nano* **2020**, *14* (5), 6181−6190.

(18) Kong, F.; Liang, C.; Wang, L.; Zheng, Y.; Perananthan, S.; Longo, R. C.; Ferraris, J. P.; Kim, M.; Cho, K. Kinetic Stability of Bulk $LiNiO_2$ and Surface Degradation by Oxygen Evolution in $LiNiO_2$-Based Cathode Materials. *Adv. Energy Mater.* **2019**, *9* (2), No. 1802586, DOI: 10.1002/aenm.201802586.

(19) Lv, Y.; Cheng, X.; Qiang, W.; Huang, B. Improved Electrochemical Performances of Ni-rich $LiNi_{0.83}Co_{0.12}Mn_{0.05}O_2$ by Mg-doping. *J. Power Sources* **2020**, *450*, No. 227718, DOI: 10.1016/j.jpowsour.2020.227718.

(20) Xu, C.; Xiang, W.; Wu, Z.; Qiu, L.; Ming, Y.; Yang, W.; Yue, L.; Zhang, J.; Zhong, B.; Guo, X.; Wang, G.; Liu, Y. Dual-site Lattice Modification Regulated Cationic Ordering for Ni-rich Cathode towards Boosted Structural Integrity and Cycle Stability. *Chem. Eng. J.* **2021**, *403*, No. 126314.

(21) Han, B.; Xu, S.; Zhao, S.; Lin, G.; Feng, Y.; Chen, L.; Ivey, D. G.; Wang, P.; Wei, W. Enhancing the Structural Stability of Ni-Rich Layered Oxide Cathodes with a Preformed Zr-Concentrated Defective Nanolayer. *ACS Appl. Mater. Interfaces* **2018**, *10* (46), 39599−39607.

(22) Jamil, S.; Li, C.; Fasehullah, M.; Liu, P.; Xiao, F.; Wang, H.; Bao, S.; Xu, M. Ni/Li Antisite Induced Disordered Passivation Layer for High-Ni Layered Oxide Cathode Material. *Energy Storage Mater.* **2022**, *45*, 720−729, DOI: 10.1016/j.ensm.2021.12.025.

(23) Kim, U. H.; Jun, D. W.; Park, K. J.; Zhang, Q.; Kaghazchi, P.; Aurbach, D.; Major, D. T.; Goobes, G.; Dixit, M.; Leifer, N.; Wang, C. M.; Yan, P.; Ahn, D.; Kim, K. H.; Yoon, C. S.; Sun, Y. K. Pushing the Limit of Layered Transition Metal Oxide Cathodes for High-energy Density Rechargeable Li Ion Batteries. *Energy Environ. Sci.* **2018**, *11* (5), 1271−1279.

(24) Zheng, Y.; Zhang, R.; Vanaphuti, P.; Liu, Y.; Yang, Z.; Wang, Y. Positive Role of Fluorine Impurity in Recovered $LiNi_{0.6}Co_{0.2}Mn_{0.2}O_2$ Cathode Materials. *ACS Appl. Mater. Interfaces* **2021**, *13* (48), 57171−57181.

(25) Zhang, H.-L.; Liu, S. Synthesis and Characterization of $LiNi_{1/3}Co_{1/3}Mn_{1/3}O_{2-x}Cl_x$ as Cathode Materials for Lithium Ion Batteries at 55°C. *Adv. Mater. Sci. Eng.* **2013**, *2013*, No. 375074, DOI: 10.1155/2013/375074.

(26) Li, J.; Wu, J.; Li, S.; Liu, G.; Cui, Y.; Dong, Z.; Liu, H.; Sun, X. Stabilizing $LiNi_{0.8}Co_{0.15}Mn_{0.05}O_2$ Cathode by Doping Sulfate for Lithium-Ion Batteries. *ChemSusChem* **2021**, *14* (13), 2721−2730.

(27) Yu, H.; Zhu, H.; Yang, Z.; Liu, M.; Jiang, H.; Li, C. Bulk Mg-doping and Surface Polypyrrole-coating Enable High-rate and Long-life for Ni-rich Layered Cathodes. *Chem. Eng. J.* **2021**, *412*, No. 128625.

(28) Park, G.-T.; Yoon, D. R.; Kim, U.-H.; Namkoong, B.; Lee, J.; Wang, M. M.; Lee, A. C.; Gu, X. W.; Chueh, W. C.; Yoon, C. S.; Sun, Y.-K. Ultrafine-grained Ni-rich Layered Cathode for Advanced Li-ion Batteries. *Energy Environ. Sci.* **2021**, *14* (12), 6616−6626.

(29) Ryu, H.-H.; Lim, H.-W.; Kang, G.-C.; Park, N.-Y.; Sun, Y.-K. Long-Lasting Ni-Rich NCMA Cathodes via Simultaneous Microstructural Refinement and Surface Modification. *ACS Energy Lett.* **2023**, *8* (3), 1354−1361.

(30) Zhou, Y.; Zhang, H.; Wang, Y.; Wan, T.; Guan, P.; Zhou, X.; Wang, X.; Chen, Y.; Shi, H.; Dou, A.; Su, M.; Guo, R.; Liu, Y.; Dai, L.; Chu, D. Relieving Stress Concentration through Anion−Cation Codoping toward Highly Stable Nickel-Rich Cathode. *ACS Nano* **2023**, *7* (20), 20621−20633, DOI: 10.1021/acsnano.3c07655.

(31) Ou, X.; Liu, T.; Zhong, W.; Fan, X.; Guo, X.; Huang, X.; Cao, L.; Hu, J.; Zhang, B.; Chu, Y. S.; Hu, G.; Lin, Z.; Dahbi, M.; Alami, J.; Amine, K.; Yang, C.; Lu, J. Enabling High Energy Lithium Metal Batteries via Single-crystal Ni-rich Cathode Material Co-doping Strategy. *Nat. Commun.* **2022**, *13* (1), No. 2319, DOI: 10.1038/s41467-022-30020-4.

(32) Sun, Y.; Wang, C.; Huang, W.; Zhao, G.; Duan, L.; Liu, Q.; Wang, S.; Fraser, A.; Guo, H.; Sun, X. One-Step Calcination Synthesis of Bulk-Doped Surface-Modified Ni-Rich Cathodes with Superlattice for Long-Cycling Li-Ion Batteries. *Angew. Chem., Int. Ed.* **2023**, *62* (20), No. e202300962, DOI: 10.1002/anie.202300962.

(33) Sun, H. H.; Kim, U.-H.; Park, J.-H.; Park, S.-W.; Seo, D.-H.; Heller, A.; Mullins, C. B.; Yoon, C. S.; Sun, Y.-K. Transition Metal-doped Ni-rich Layered Cathode Materials for Durable Li-ion Batteries. *Nat. Commun.* **2021**, *12* (1), No. 6552, DOI: 10.1038/s41467-021-26815-6.

(34) Kresse, G.; Furthmüller, J. Efficient Iterative Schemes for Ab Initio Total-energy Calculations Using a Plane-wave Basis Set. *Phys. Rev. B* **1996**, *54* (16), 11169−11186.

(35) Perdew, J. P.; Burke, K.; Ernzerhof, M. Generalized Gradient Approximation Made Simple. *Phys. Rev. Lett.* **1996**, *77* (18), 3865−3868.

(36) Blöchl, P. E. Projector Augmented-wave Method. *Phys. Rev. B* **1994**, *50* (24), 17953−17979.

(37) Grimme, S.; Antony, J.; Ehrlich, S.; Krieg, H. A Consistent and Accurate Ab Initio Parametrization of Density Functional Dispersion Correction (DFT-D) for the 94 Elements H-Pu. *J. Chem. Phys.* **2010**, *132* (15), No. 154104, DOI: 10.1063/1.3382344.

(38) Henkelman, G.; Uberuaga, B. P.; Jónsson, H. A Climbing Image Nudged Elastic Band Method for Finding Saddle Points and Minimum Energy Paths. *J. Chem. Phys.* **2000**, *113* (22), 9901−9904.

(39) Kim, D. H.; Song, J. H.; Jung, C. H.; Eum, D.; Kim, B.; Hong, S. H.; Kang, K. Stepwise Dopant Selection Process for High-Nickel Layered Oxide Cathodes. *Adv. Energy Mater.* **2022**, *12* (18), No. 2200136, DOI: 10.1002/aenm.202200136.

(40) Guo, Y. J.; Zhang, C. H.; Xin, S.; Shi, J. L.; Wang, W. P.; Fan, M.; Chang, Y. X.; He, W. H.; Wang, E.; Zou, Y. G.; Yang, Xa.; Meng, F.; Zhang, Y. Y.; Lei, Z. Q.; Yin, Y. X.; Guo, Y. G. Competitive Doping Chemistry for Nickel-Rich Layered Oxide Cathode Materials. *Angew. Chem., Int. Ed.* **2022**, *61* (21), No. e202116865, DOI: 10.1002/anie.202116865.

(41) Li, J.; Zhong, W.; Deng, Q.; Zhang, Q.; Lin, Z.; Yang, C. Mechanistic Origin for High Structural Stability of Single Crystalline Nickel-Rich Cathode Materials Via Al and Sm Co-Doping. *Adv. Funct. Mater.* **2023**, *33* (24), No. 2300127, DOI: 10.1002/adfm.202300127.

(42) Zhao, S.; Wang, B.; Zhang, Z.; Zhang, X.; He, S.; Yu, H. First-principles Computational Insights into Lithium Battery Cathode Materials. *Electrochem. Energy Rev.* **2022**, *5* (1), 1−31.

(43) Zhu, H.; Wang, Z.; Chen, L.; Hu, Y.; Jiang, H.; Li, C. Strain Engineering of Ni-Rich Cathode Enables Exceptional Cyclability in Pouch-Type Full Cells. *Adv. Mater.* **2022**, *35* (9), No. 2209357, DOI: 10.1002/adma.202209357.

(44) Kim, U.-H.; Park, G.-T.; Son, B.-K.; Nam, G. W.; Liu, J.; Kuo, L.-Y.; Kaghazchi, P.; Yoon, C. S.; Sun, Y.-K. Heuristic Solution for Achieving Long-term Cycle Stability for Ni-rich Layered Cathodes at Full Depth of Discharge. *Nat. Energy* **2020**, *5* (11), 860−869.

(45) Qiu, Q.-Q.; Shadike, Z.; Wang, Q.-C.; Yue, X.-Y.; Li, X.-L.; Yuan, S.-S.; Fang, F.; Wu, X.-J.; Hunt, A.; Waluyo, I.; Bak, S.-M.; Yang, X.-Q.; Zhou, Y.-N. Improving the Electrochemical Performance and Structural Stability of the $LiNi_{0.8}Co_{0.15}Al_{0.05}O_2$ Cathode Material at High-Voltage Charging through Ti Substitution. *ACS Appl. Mater. Interfaces* **2019**, *11* (26), 23213−23221.

(46) Yu, H.; Cao, Y.; Chen, L.; Hu, Y.; Duan, X.; Dai, S.; Li, C.; Jiang, H. Surface Enrichment and Diffusion Enabling Gradient-doping and Coating of Ni-rich Cathode toward Li-ion Batteries. *Nat. Commun.* **2021**, *12* (1), No. 4564, DOI: 10.1038/s41467-021-24893-0.

(47) Moshtev, R. V.; Zlatilova, P.; Manev, V.; Sato, A. The $LiNiO_2$ Solid Solution as a Cathode Material for Rechargeable Lithium Batteries. *J. Power Sources* **1995**, *54* (2), 329−333.

(48) Huang, Z.-X.; Zhang, X.-L.; Zhao, X.-X.; Heng, Y.-L.; Wang, T.; Geng, H.; Wu, X.-L. Hollow $Na_{0.62}K_{0.05}Mn_{0.7}Ni_{0.2}Co_{0.1}O_2$ Polyhedra with Exposed Stable {001} Facets and K Riveting for Sodium-ion Batteries. *Sci. China Mater.* **2023**, *66* (1), 79−87.

(49) Wei, T.-T.; Liu, X.; Yang, S.-J.; Wang, P.-F.; Yi, T.-F. Regulating the Electrochemical Activity of Fe-Mn-Cu-based Layer Oxides as Cathode Materials for High-performance Na-ion Battery. *J. Energy Chem.* **2023**, *80*, 603−613.

(50) Zhang, Q.; Deng, Q.; Zhong, W.; Li, J.; Wang, Z.; Dong, P.; Huang, K.; Yang, C. Tungsten Boride Stabilized Single-Crystal

$LiNi_{0.83}Co_{0.07}Mn_{0.1}O_2$ Cathode for High Energy Density Lithium-Ion Batteries: Performance and Mechanisms. *Adv. Funct. Mater.* **2023**, *33* (27), No. 2301336, DOI: 10.1002/adfm.202301336.

(51) Yi, T. F.; Shi, L.; Han, X.; Wang, F.; Zhu, Y.; Xie, Y. Approaching High-Performance Lithium Storage Materials by Constructing Hierarchical $CoNiO_2$@CeO_2 Nanosheets. *Energy Environ. Mater.* **2021**, *4* (4), 586−595.

(52) Wei, T.-T.; Peng, P.; Ji, Y.-R.; Zhu, Y.-R.; Yi, T.-F.; Xie, Y. Rational Construction and Decoration of $Li_5Cr_7Ti_6O_{25}$@C Nanofibers as Stable Lithium Storage Materials. *J. Energy Chem.* **2022**, *71*, 400−410.

(53) Yi, T.-F.; Qiu, L.-Y.; Mei, J.; Qi, S.-Y.; Cui, P.; Luo, S.; Zhu, Y.-R.; Xie, Y.; He, Y.-B. Porous spherical NiO@$NiMoO_4$@PPy Nanoarchitectures as Advanced Electrochemical Pseudocapacitor Materials. *Sci. Bull.* **2020**, *65* (7), 546−556.

(54) Zou, Y. G.; Mao, H.; Meng, X. H.; Du, Y. H.; Sheng, H.; Yu, X.; Shi, J. L.; Guo, Y. G. Mitigating the Kinetic Hindrance of Single-Crystalline Ni-Rich Cathode via Surface Gradient Penetration of Tantalum. *Angew. Chem., Int. Ed.* **2021**, *60* (51), 26535−26539.

(55) Jamil, S.; Bin Yousaf, A.; Hee Yoon, S.; Suk Han, D.; Yang, L.; Kasak, P.; Wang, X. Dual Cationic Modified High Ni-low Co Layered Oxide Cathode with a Heteroepitaxial Interface for High Energy-density Lithium-ion Batteries. *Chem. Eng. J.* **2021**, *416*, No. 129118.

(56) Yang, Z.; Chen, L.; Zhu, H.; Zhu, Y.; Jiang, H.; Li, C. Stabilizing Surface Chemistry and Texture of Single-crystal Ni-rich Cathodes for Li-ion Batteries. *J. Mater. Sci. Technol.* **2022**, *125*, 192−197.

(57) Hwang, D.-Y.; Kim, H.-S.; Lee, S.-H. Highly Stable and High-performance $MgHPO_4$ Surface-modified Ni-rich Cathode Materials for Advanced Lithium Ion Batteries. *J. Mater. Chem. A* **2022**, *10* (31), 16555−16569.

(58) Zhang, Y.; Song, Y.; Liu, J. Double Conductor Coating to Improve the Structural Stability and Electrochemical Performance of $LiNi_{0.8}Co_{0.1}Mn_{0.1}O_2$ Cathode Material. *ACS Sustainable Chem. Eng.* **2023**, *11* (6), 2264−2274.

(59) Lu, S.-Q.; Zhang, Q.; Meng, F.; Liu, Y.-N.; Mao, J.; Guo, S.; Qi, M.-Y.; Xu, Y.-S.; Qiao, Y.; Zhang, S.-D.; Jiang, K.; Gu, L.; Xia, Y.; Chen, S.; Chen, G.; Cao, A.-M.; Wan, L.-J. Surface Lattice Modulation through Chemical Delithiation toward a Stable Nickel-Rich Layered Oxide Cathode. *J. Am. Chem. Soc.* **2023**, *145* (13), 7397−7407.

(60) Cai, J.; Yang, Z.; Zhou, X.; Wang, B.; Suzana, A.; Bai, J.; Liao, C.; Liu, Y.; Chen, Y.; Song, S.; Zhang, X.; Wang, L.; He, X.; Meng, X.; Karami, N.; Ali Shaik Sulaiman, B.; Chernova, N. A.; Upreti, S.; Prevel, B.; Wang, F.; Chen, Z. Unveiling the Parasitic-Reaction-driven Surface Reconstruction in Ni-rich Cathode and the Electrochemical Role of Li_2CO_3. *J. Energy Chem.* **2023**, *85*, 126−136.

(61) Li, L.; Zhang, Y.; Hu, N.; Wang, K.; Liu, Y.; Wang, X.; Zhou, X.; Ma, J.; Cui, G. Carbonized Polymer Dots Enhancing Interface Stability of $LiNi_{0.8}Co_{0.1}Mn_{0.1}O_2$ Cathodes. *Adv. Mater. Interfaces* **2023**, *10* (20), No. 2300254, DOI: 10.1002/admi.202300254.

(62) Hao, Y.; Li, X.; Liu, W.; Wang, J.; Shan, H.; Li, W.; Liu, X.; Lin, L.; Wang, X.; Sun, X. Depolarization of Li-rich Mn-based Oxide via Electrochemically Active Prussian Blue Interface Providing Superior Rate Capability. *Carbon Energy* **2022**, *5* (5), No. e272, DOI: 10.1002/cey2.272.

(63) Gu, Z.-Y.; Heng, Y.-L.; Guo, J.-Z.; Cao, J.-M.; Wang, X.-T.; Zhao, X.-X.; Sun, Z.-H.; Zheng, S.-H.; Liang, H.-J.; Li, B.; Wu, X.-L. Nano Self-assembly of Fluorophosphate Cathode Induced by Surface Energy Evolution towards High-rate and Stable Sodium-ion Batteries. *Nano Res.* **2023**, *16* (1), 439−448.

(64) Wang, J.; Yi, Z.; Liu, C.; He, M.; Miao, C.; Li, J.; Xu, G.; Xiao, W. Revealing the Effect of Nb^{5+} on the Electrochemical Performance of Nickel-rich Layered $LiNi_{0.83}Co_{0.11}Mn_{0.06}O_2$ Oxide Cathode for Lithium-ion Batteries. *J. Colloid Interface Sci.* **2023**, *635*, 295−304.

(65) Ryu, H. H.; Park, N. Y.; Yoon, D. R.; Kim, U. H.; Yoon, C. S.; Sun, Y. K. New Class of Ni-Rich Cathode Materials $Li[Ni_xCo_yB_{1-x-y}]O_2$ for Next Lithium Batteries. *Adv. Energy Mater.* **2020**, *10* (25), No. 20000495, DOI: 10.1002/aenm.202000495.

(66) Liang, Z.; Ren, M.; Guo, Y.; Zhang, T.; Gao, X.; Ma, H.; Li, F. Depressed P3−O3′ Phase Transition in an O3-type Layered Cathode for Advanced Sodium-ion Batteries. *Inorg. Chem. Front.* **2023**, *10* (24), 7187−7192.

(67) Huang, Z.-X.; Zhang, X.-L.; Zhao, X.-X.; Lü, H.-Y.; Zhang, X.-Y.; Heng, Y.-L.; Geng, H.; Wu, X.-L. Suppressing Oxygen Redox in Layered Oxide Cathode of Sodium-ion Batteries with Ribbon Superstructure and Solid-solution Behavior. *J. Mater. Sci. Technol.* **2023**, *160*, 9−17.

(68) Ryu, H. H.; Park, K. J.; Yoon, D. R.; Aishova, A.; Yoon, C. S.; Sun, Y. K. $Li[Ni_{0.9}Co_{0.09}W_{0.01}]O_2$: A New Type of Layered Oxide Cathode with High Cycling Stability. *Adv. Energy Mater.* **2019**, *9* (44), No. 1902698, DOI: 10.1002/aenm.201902698.

(69) Bai, P.; Ji, X.; Zhang, J.; Zhang, W.; Hou, S.; Su, H.; Li, M.; Deng, T.; Cao, L.; Liu, S.; He, X.; Xu, Y.; Wang, C. Formation of LiF-rich Cathode-Electrolyte Interphase by Electrolyte Reduction. *Angew. Chem., Int. Ed.* **2022**, *61* (26), No. e202202731, DOI: 10.1002/anie.202202731.

https://doi.org/10.1021/acs.iecr.3c04271
Ind. Eng. Chem. Res. 2024, 63, 2740−2749